

Deep and fast live imaging with two-photon scanned light-sheet microscopy

Thai V Truong, Willy Supatto, Davis S Koos, John M Choi & Scott E Fraser

Supplementary Figure 1	2p-SPIM setup and spatial resolution characterization.
Supplementary Figure 2	Demonstration of signal rate of 2p-SPIM at low average input power.
Supplementary Figure 3	Comparison of illumination and detection optical paths for the three imaging modalities.
Supplementary Figure 4	Comparison of image axial resolution in early fly embryos.
Supplementary Figure 5	Analysis of spatial frequency components in Fourier space: definition and application of useful contrast metric.
Supplementary Figure 6	Comparison of multi-view imaging with 2p-SPIM and 1p-SPIM.
Supplementary Figure 7	Long term non-photodamaging 4D imaging of fly development with 2p-SPIM.
Supplementary Figure 8	Fast non-phototoxic 2p-SPIM imaging of zebrafish beating heart.
Supplementary Figure 9	Combined SHG-SPIM and 2p-SPIM imaging of mouse tail.
Supplementary Table 1	Imaging parameters for all the presented images and videos.
Supplementary Results 1	Resolution characterization.
Supplementary Results 2	Similar signal rate of 2p-SPIM and 2p-LSM.
Supplementary Results 3	Quantification of imaging depth via analysis of images in Fourier space.
Supplementary Results 4	Analysis of fly photodamage experiments
Supplementary Results 5	Second harmonic generation scanned light-sheet microscopy.
Supplementary Discussion 1	Resolution and field of view in 2p- and 1p-SPIM.
Supplementary Discussion 2	Advantages of the scanned light sheet versus static light sheet for 2p-SPIM.
Supplementary Discussion 3	Low photodamage of 2p-SPIM allows high speed imaging.
Supplementary Discussion 4	Comparison of 2p-SPIM with other imaging techniques.

Note: Supplementary Videos 1–7 are available on the Nature Methods website.

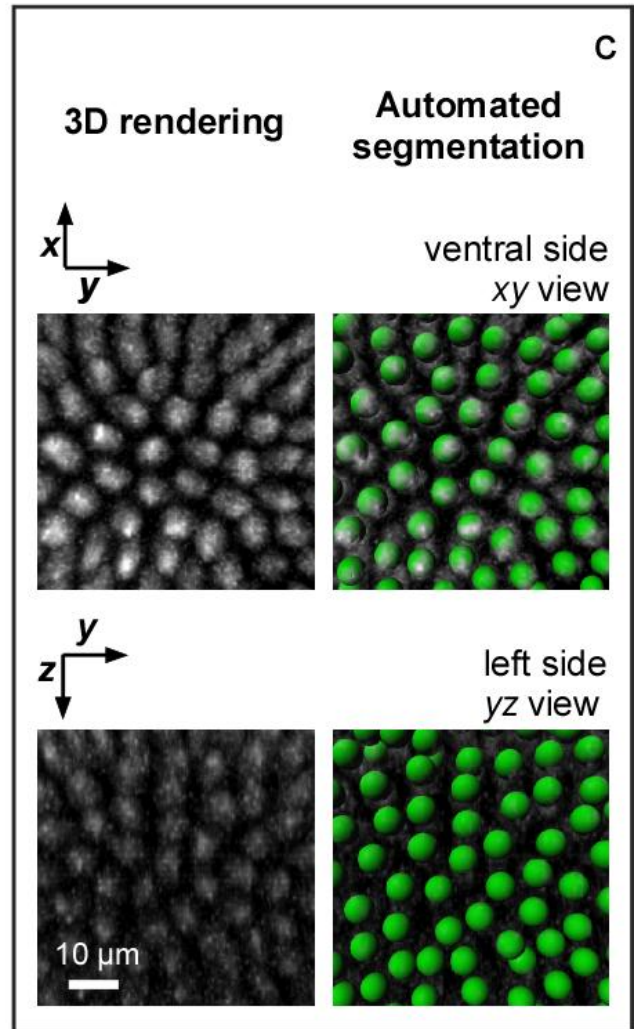
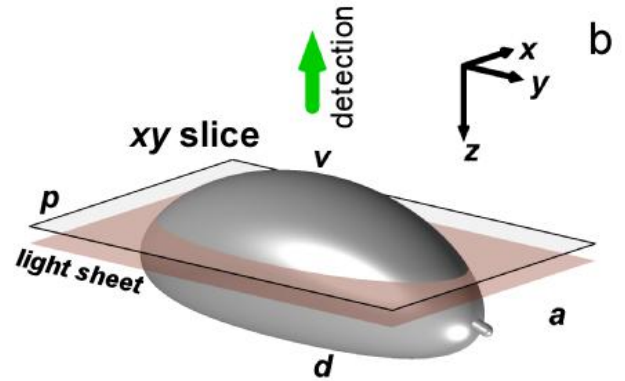
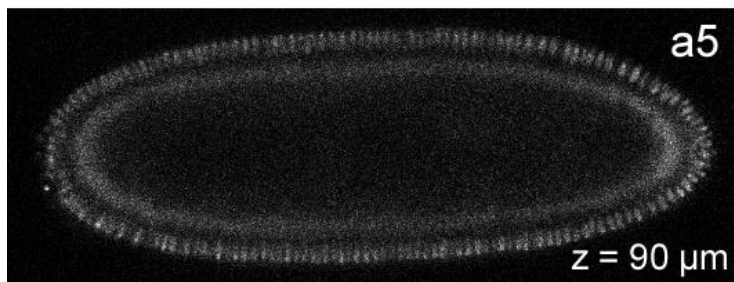
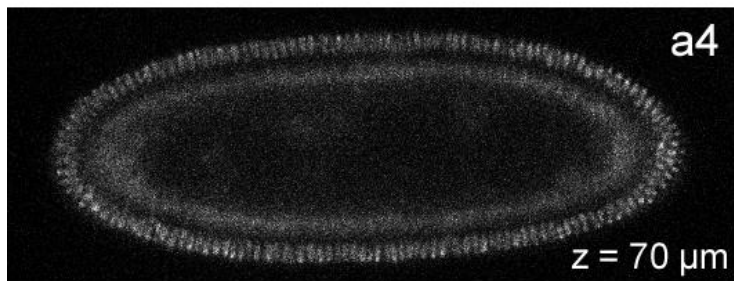
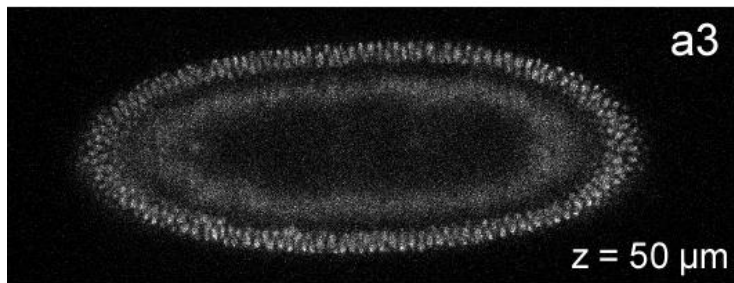
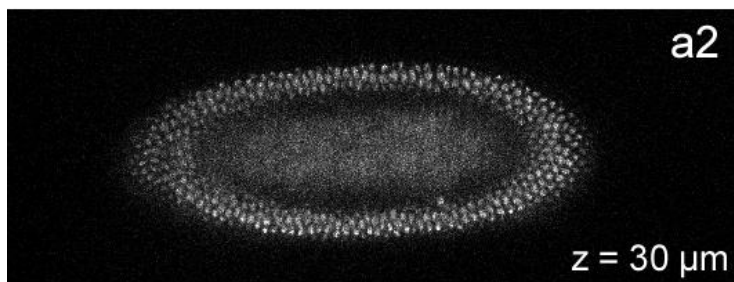
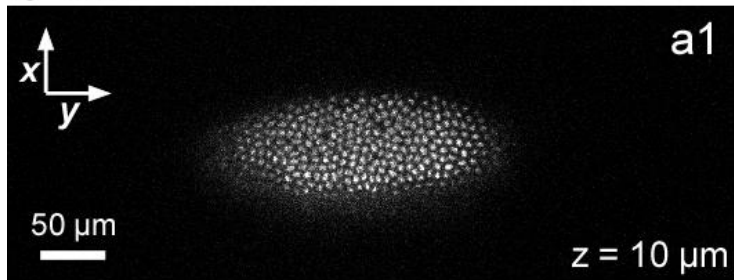
Supplementary Figure 1

2p-SPIM setup and spatial resolution characterization

(a) Schematic of the main components of the two photon scanned light-sheet microscopy setup. Following the beam path from the laser light sources: ND: neutral density filter; MS: mechanical shutter; M: mirror; PC: Pockel's cell; DM: dichroic mirror; GV: galvanometer scanner; SL: scan lens; TL: tube lens; BS: beamsplitter, 50/50, broadband; IO: illumination objective lens; SC: sample chamber; S: sample; DO: detection objective lens; F: optical filter(s); SM: switching mirror; EP: eyepieces; EM-CCD: electron-multiplying charged coupled device camera. (b) Imaging performance parameters of setup: maximum intensity projections of representative xz-slices (x and z directions are along the horizontal and vertical axes, respectively) of sub-diffraction fluorescent beads imaged by 2p-SPIM (b1), 1p-SPIM (b2), and 2p-LSM (b3). Images were computationally oversampled and presented in fire color map to enhance visualization. Scale bar in (b), 3 μm .

Supplementary Figure 2
Demonstration of signal rate of 2p-SPIM at low average input power

xy slice



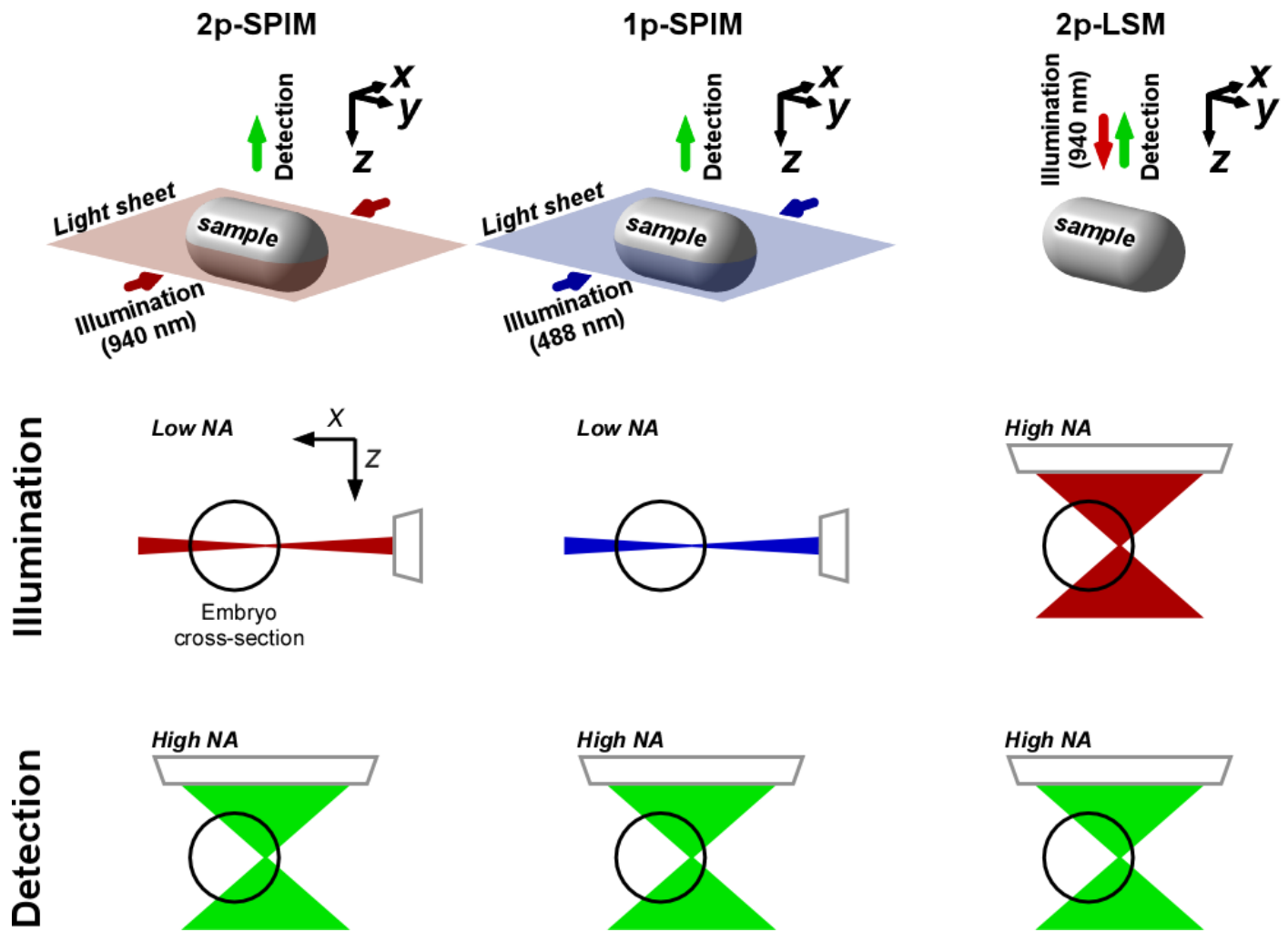
Supplementary Figure 2

Demonstration of signal rate of 2p-SPIM at low average input power

Signal level of 2p-SPIM using ~30 mW excitation light and 1 sec frame time (approximately equivalent to the typical conditions used in 2p-LSM). **(a)** shows xy-slices at different z-planes (**a1-5**) of a fly embryo (stage 5) imaged with the ventral side facing the detection objective and the light-sheet along the xy-plane entering the embryos from lateral sides **(b)**. At this level of average laser power, the signal to noise ratio is sufficient for automated segmentation of nuclei using standard software (Imaris, Bitplane) **(c)** both on the ventral nuclei **(c, up)** and the lateral side **(c, down)**.

Supplementary Figure 3

Comparison of illumination and detection optical paths for the three imaging modalities



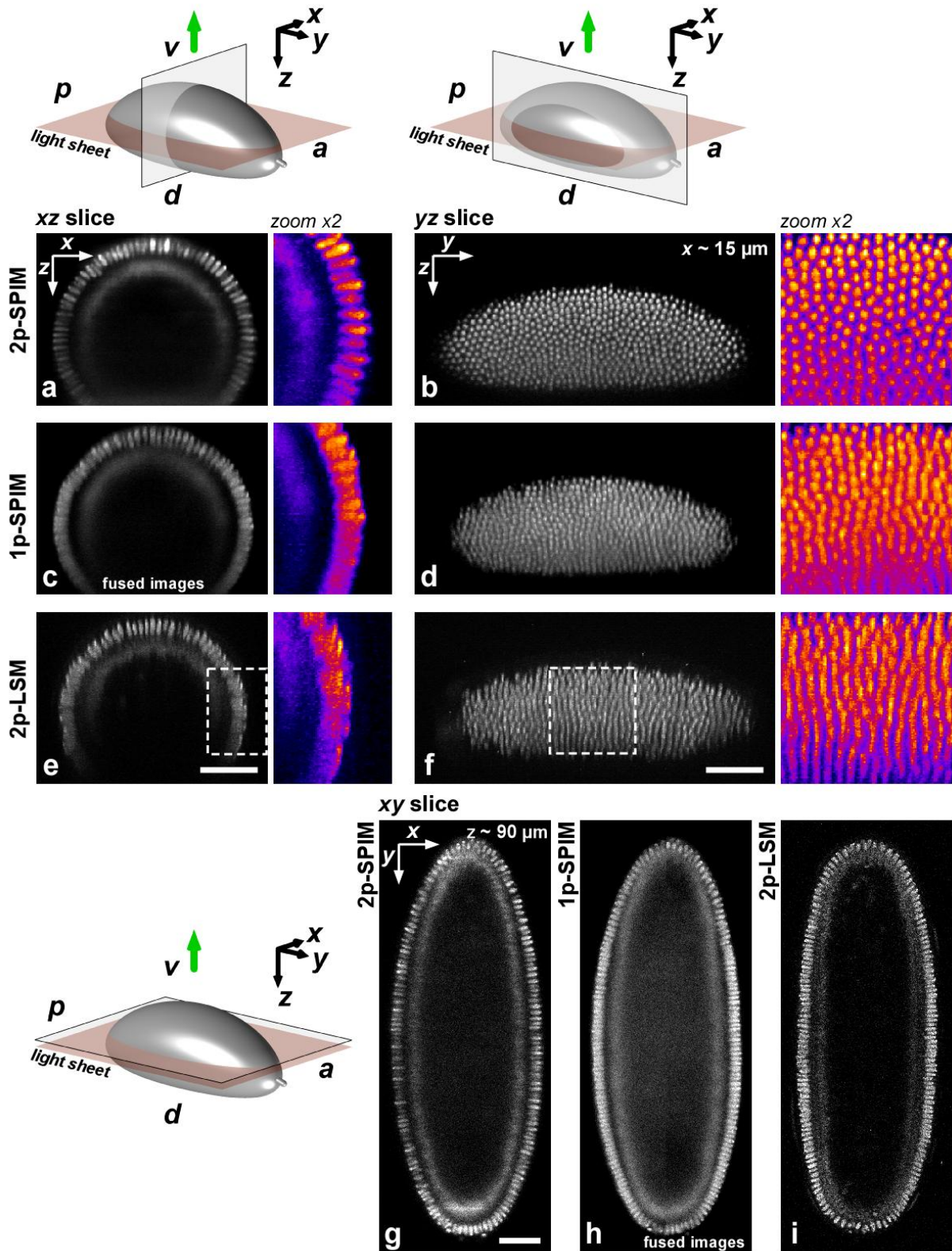
Supplementary Figure 3

Comparison of illumination and detection optical paths for the three imaging modalities

For all imaging modalities, the image focal plane is parallel to the xy -plane, with the cylindrically-shaped fly embryo mounted so that its long axis is parallel to the y -direction. For 2p-LSM, illumination and detection are both along the z -axis. For the SPIM modalities, the x -propagating illumination light-sheet traverses the sample and creates optical sections along the xy -plane, which then is imaged by the camera (not shown) oriented with its optical axis along the z -direction. Z-stack imaging is done by moving the sample across the light-sheet along the z -direction. All SPIM data presented in our study were collected with this geometry, with the only difference in which side of the embryo (ventral, dorsal, lateral) was oriented (via rotation about the y -axis) to face the detection objective. Note that while the sample depth for 2p-LSM is simply the distance along the axial (z) direction, for 2p- and 1p-SPIM, there are two depths, one along the illumination (x , lateral) direction and one along the detection (z , axial) direction. Minimizing the sum of these two depths in SPIM is critical for obtaining the best image quality. The bidirectional illumination was adjusted so that the two nominal fields of view span the entire x -depth of the sample, overlapping slightly at the center, ensuring that the illumination depth does not exceed half of the sample. The detection depth could also be made to not exceed half of the sample by multi-view imaging, where the sample is imaged with at least 2 opposing z -stacks by rotating the sample about the y -axis by 180° .

For 2p- and 1p-SPIM, low NA is used for illumination (along x -axis) and high NA is used for detection (along z -axis). For 2p-LSM, illumination and detection (both along z -axis) are done using the same high NA objective lens. The high illumination NA of 2p-LSM necessarily means that the focusing solid angle encompasses a large volume of the sample, making it susceptible to aberration effects due to sample optical inhomogeneity. For example, for the region towards the side of the sample (as shown in the figure above), approximately half of the focusing solid angle goes through water and the other half goes through the embryo. Aberration effects would then cause the focal volume to be significantly larger than the diffraction limit, leading to a loss of resolution. In contrast, for 2p-SPIM, the smaller focusing solid angle of the low-NA illumination would produce much less sensitivity to aberration effects.

Supplementary Figure 4
Comparison of image axial resolution in early fly embryos



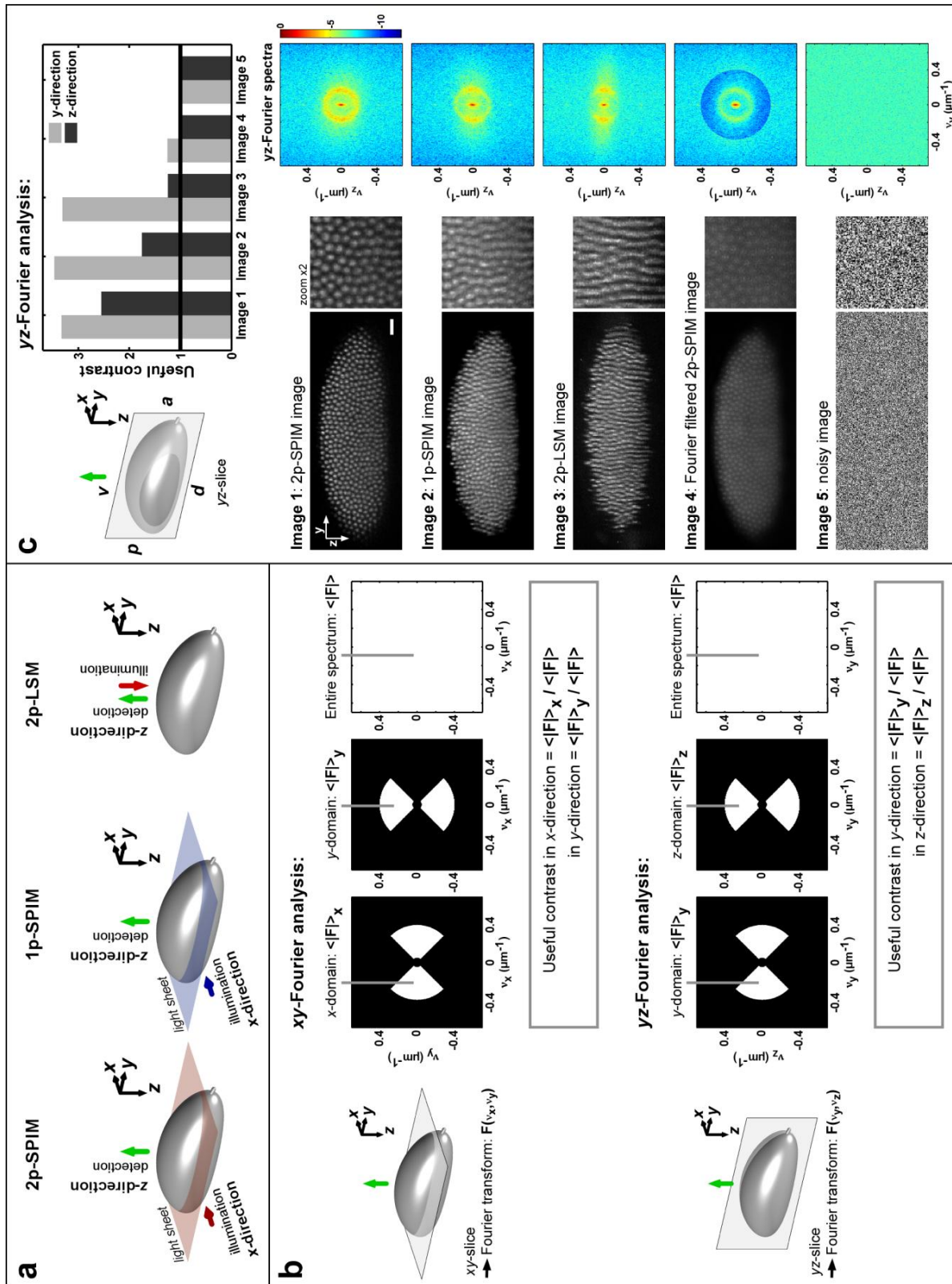
Supplementary Figure 4

Comparison of image axial resolution in early fly embryos

Stage 5 H2A-GFP fly embryos imaged with 2p-SPIM (**a-b, g**), 1p-SPIM (**c-d, h**), and 2p-LSM (**e-f, i**), with 2x-zoomed view of the dashed boxed area using ImageJ fire color map to enhance contrast. (**a, c, e**) xz-slices comparing the cellular resolution around the embryo. (**b, d, f**) yz-slices showing the cellular resolution on the lateral side of the embryo at $x \sim 15 \mu\text{m}$ from embryo surface. While all three techniques resolve well cell nuclei located on the ventral side of the embryo, nearest to the detection objective (upper part in **a, c** and **e**), for nuclei deeper in the axial direction along the two lateral sides of embryo, there was a dramatic improvement in the resolution of 2p-SPIM (**a**) over the other techniques (**c** and **e**). The degradation of axial resolution clearly revealed in yz-slices result in apparent elongated shape of nuclei in the z-direction, especially for 2p-LSM (**f**), whereas good resolution is maintained when using 2p-SPIM (**b**). These observations are demonstrated using quantitative analysis in **Supplementary Fig. 5c**. (**g-i**) xy-slices at the middle of the embryo ($z \sim 90 \mu\text{m}$ from embryo surface) demonstrate that the best lateral resolution is achieved by 2p-LSM, followed by 2p-SPIM and then 1p-SPIM. The sparser signal in 2p-SPIM image, compared with 1p-SPIM and 2p-LSM, indicates higher axial resolution and better optical sectioning, as nuclei are distributed at slightly different z-positions. The same embryo was imaged using 2p-SPIM and 1p-SPIM with the ventral side facing the detection objective and the light-sheet along the xy-plane entering the embryos from lateral sides. Similarly-staged embryo was imaged in 2p-LSM with the ventral side facing the excitation/detection objective. Sample schematics: red plane denotes the light-sheet, gray plane denotes the computational slice of the 3D dataset shown in the corresponding images, and green arrow denotes the signal detection direction. 1p-SPIM images obtained with sequential bidirectional illumination and fusion of 2 datasets from each side. 2p-SPIM images obtained with simultaneous bidirectional illumination. *a*: anterior, *p*: posterior, *d*: dorsal, *v*: ventral. Scale bar, 50 μm .

Supplementary Figure 5

Analysis of spatial frequency components in Fourier space: definition and application of useful contrast metric

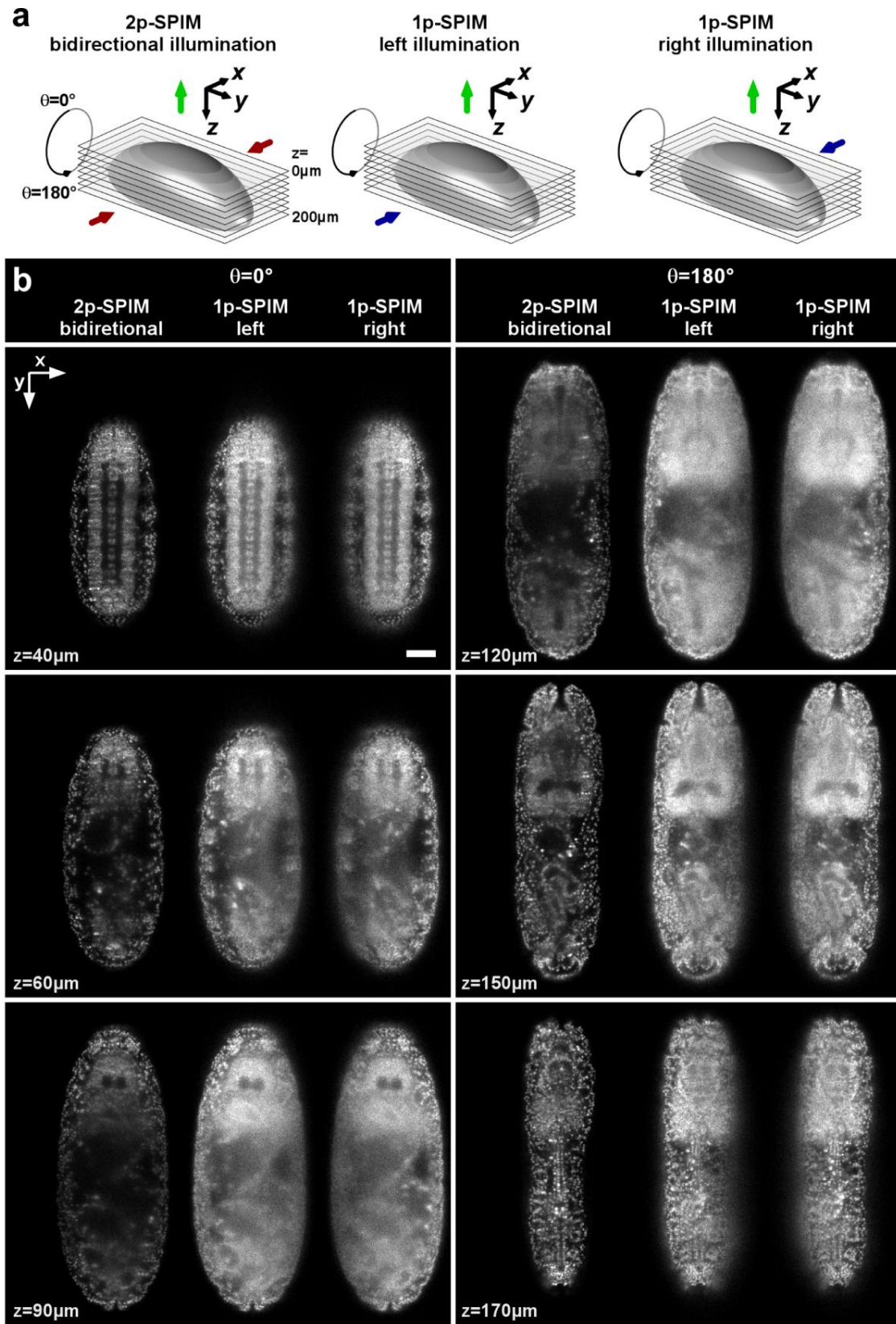


Supplementary Figure 5

Analysis of spatial frequency components in Fourier space: definition and application of useful contrast metric

(a) Schematics showing the directions of detection and illumination for the three imaging modalities. Imaging performance and depth penetration are investigated either in the detection z -direction (from z -stacks of xy -slices) or in the illumination x -direction (from x -stacks of yz -slices). (b) Definition of useful contrast metric based on xy - or yz -Fourier analysis (in the detection or illumination directions, respectively). In the case of xy -Fourier analysis (upper part of b), the Fourier transform $F(v_x, v_y)$ of each xy -slice is computed, v_x and v_y being the spatial frequencies in x - and y -directions, respectively. To define a useful contrast metric in each of these spatial directions, x -domain and y -domain are defined in the xy -Fourier spectrum (white areas in the graphs) between $v = 0.05 \mu\text{m}^{-1}$ and $v = 0.4 \mu\text{m}^{-1}$ (corresponding to spatial length scales between $20 \mu\text{m}$ and $2 \mu\text{m}$). The average Fourier spectrum coefficients is computed within the x -domain ($\langle |F| \rangle_x$), the y -domain ($\langle |F| \rangle_y$), and the entire spectrum ($\langle |F| \rangle$). Finally, the useful contrasts in x - and y -direction are defined as $\langle |F| \rangle_x / \langle |F| \rangle$, and $\langle |F| \rangle_y / \langle |F| \rangle$, respectively. Similar analysis is obtained using yz -slices and yz -Fourier analysis (lower part of b). (c) The application of useful contrast metric is illustrated by comparing the analysis of 5 different sample images (data correspond to **Supplementary Fig. 4**): Image 1 (2p-SPIM), Image 2 (1p-SPIM), Image 3 (2p-LSM), Image 4 (Fourier filtered image of Image 1 for which Fourier coefficients in the $0.05 < v < 0.4 \mu\text{m}^{-1}$ range are lowered by a factor of 5), Image 5 (noisy image). Each image are represented (bottom left of c) with a $\times 2$ zoom-in and the corresponding Fourier spectra (bottom right of c). The corresponding useful contrast values in y - and z -direction are plotted in a graph (upper right of c) illustrating the main information that can be obtained using this metric. First, isotropic resolution corresponds to isotropic Fourier spectrum and identical useful contrast values in each direction. 2p-SPIM image (Image 1) appears quasi-isotropic; 1p-SPIM (Image 2) and 2p-LSM (Image 3) are clearly anisotropic with low values of useful contrast in the z -direction (axial direction) compared to the y -direction (lateral-direction). A noisy image (Image 5) exhibits values of useful contrast close to one. As expected, the filtering of Image 1 by lowering the Fourier coefficients in the frequency domains used to define the metric drastically reduced the values of useful contrast (Image 4). Importantly, the resulting image exhibits a loss of biological information: the signal from the nuclei disappears and only high-frequency noise and low-frequency background remain. Scale bar in (c), $20 \mu\text{m}$.

Supplementary Figure 6
Comparison of multi-view imaging with 2p-SPIM and 1p-SPIM



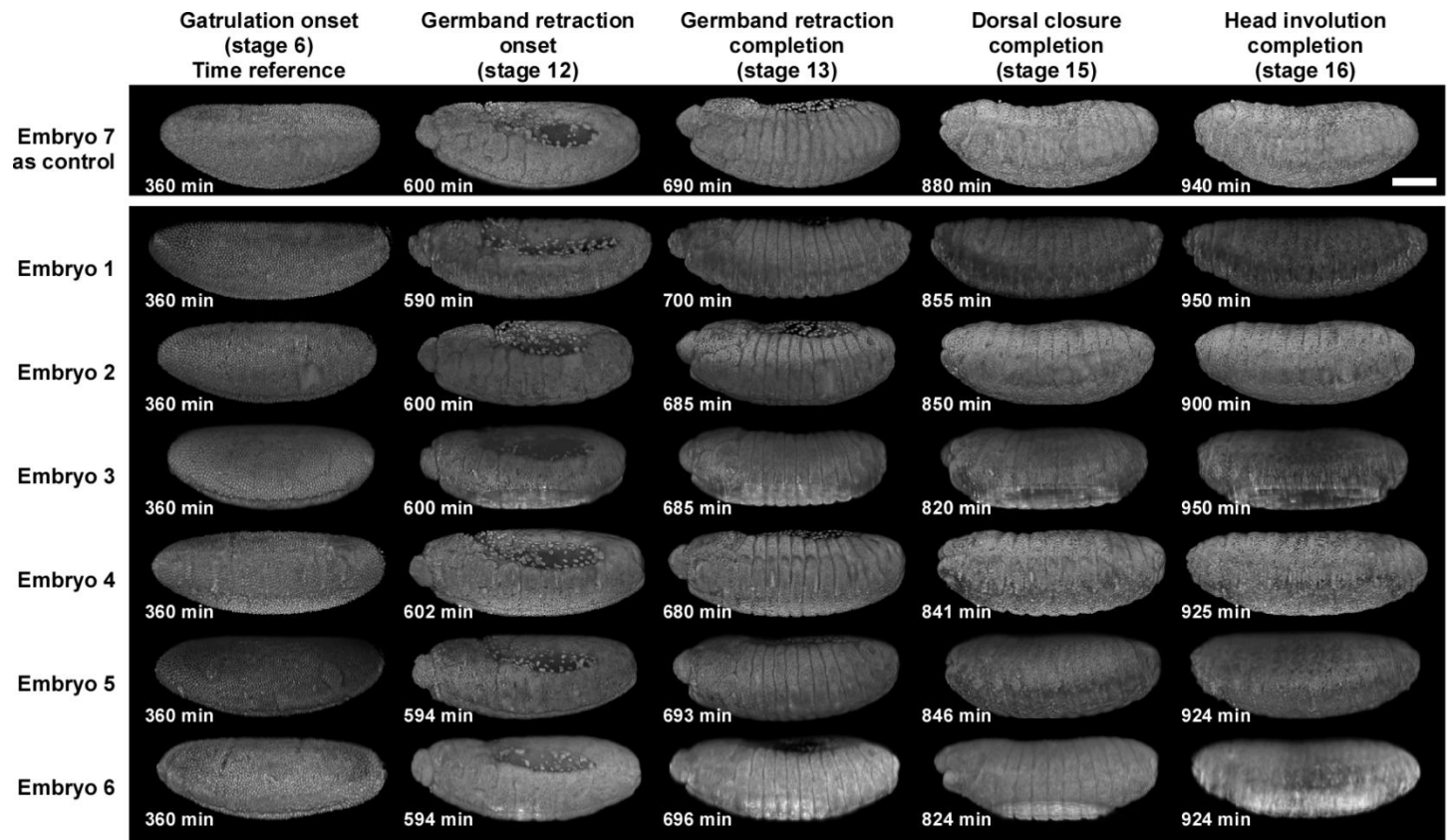
Supplementary Figure 6

Comparison of multi-view imaging with 2p-SPIM and 1p-SPIM

In multi-view imaging, multiple 3D image datasets of the same sample are collected from different orientations, and then combined computationally to yield a resulting 3D dataset with superior resolution and coverage compared with the original datasets. Multi-view imaging could be readily applied to 2p-SPIM - its improved penetration depth and lower background compared to the 1p counterpart means that less imaging views are required to capture the same 3D sample, thus minimizing acquisition time and computational processing. **(a)** Schematics illustrating how to capture the entire fly embryo by imaging from two opposing views after rotating the embryo about the y-axis ($\theta=0^\circ$ and $\theta=180^\circ$), using simultaneous bidirectional illumination 2p-SPIM (resulting in two datastacks) or sequential bidirectional illumination 1p-SPIM (resulting in four datastacks). **(b)** Resulting sample raw-images at different z-depths through the entire embryo (stage 16) acquired at $\theta=0^\circ$ (left side) or $\theta=180^\circ$ (right side). Full raw images and 3D-reconstructions are displayed in **Supplementary Videos 4** and **5**, respectively. The high image quality obtained with 2p-SPIM, with reduced background and enhanced resolution compared with 1p-SPIM, allows reconstruction of the entire embryo by simple manual stitching of the $\theta=0^\circ$ and $\theta=180^\circ$ stacks together (**Supplementary Video 6**). Note that 1p-SPIM does not have sufficient penetration depth to capture and resolve the cell nuclei at the center of the sample, regardless of how many views are employed, while 2p-SPIM does resolve a good portion of these nuclei. Scale bar in **(b)**, 50 μm .

Supplementary Figure 7

Long term non-photodamaging 4D imaging of fly development with 2p-SPIM



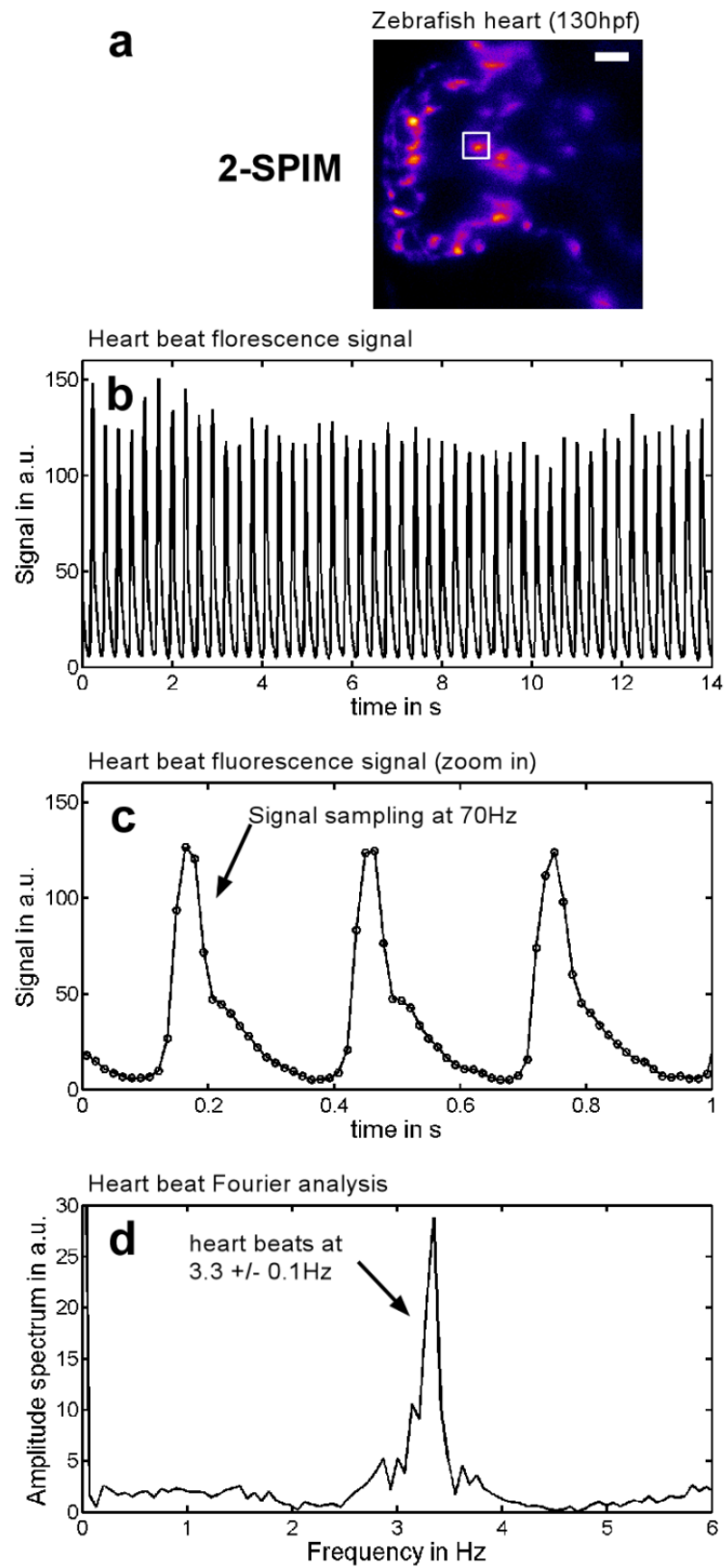
Supplementary Figure 7

Long-term non-photodamaging 4D imaging of fly development with 2p-SpIM

Representative images of embryos used for analysis in **Fig. 3**. See **Fig. 3** legend, **Online Methods**, and **Supplementary Results 4** for details. See **Fig. 2j** for representative high-resolution 3D renderings. See **Supplementary Video 3** for a sample full sequence. Embryo anterior side left, dorsal side up. Time is shown in minutes (min) after fertilization (onset of gastrulation at 180 min used as a time reference). Scale bar, 100 μm .

Supplementary Figure 8

Fast non-phototoxic 2p-SPIM imaging of zebrafish beating heart



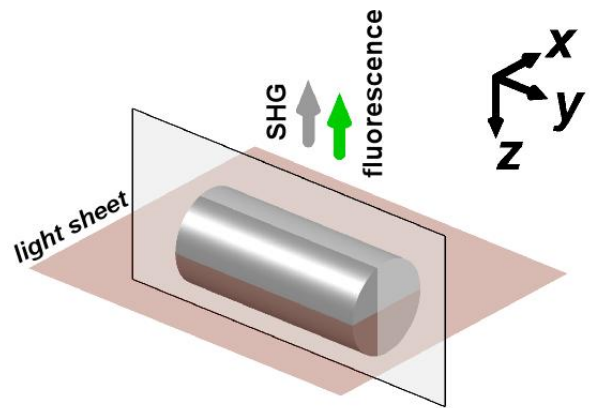
Supplementary Figure 8

Fast non-phototoxic 2p-SPIM imaging of zebrafish beating heart

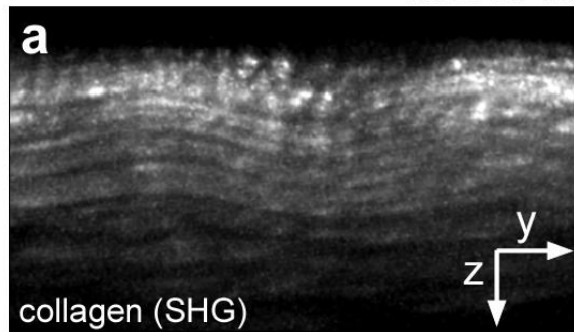
Analysis of heart beating from high-speed 2p-SPIM imaging of 5.4 day old (130 hours post fertilization) transgenic zebrafish embryo where the endocardium was labeled with GFP. Image acquisition was at 70 frames per second, for field of view of 400 x 400 pixels (corresponding to more than 11.2 million pixels per second, see **Supplementary Video 7**), using average excitation power of 50mW for a continuous duration of 14 s. The fluorescence signal is averaged in a small area of the heart, white square in **(a)**, and plotted as a function of time in **(b)**, showing the regularity of the heart beating. The variation of signal during 1s **(c)** shows that the fast acquisition rate at 70 fps allows capturing of fast motional features during each beat cycle. Fourier analysis of the time variation of the fluorescence signal over the 14-s time interval **(d)** shows a sharp peak at 3.3 Hz, demonstrating further the regular, non-phototoxic, heart beating during the entire acquisition period. This heart rate is within the normal range recorded previously in literature²⁴. Scale bar in **(a)**, 20 μm .

Supplementary Figure 9

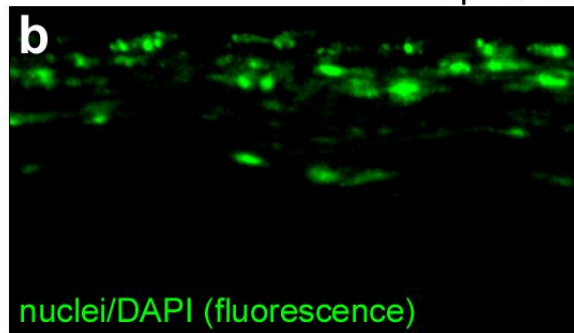
Combined SHG-SPIM and 2p-SPIM imaging of mouse tail



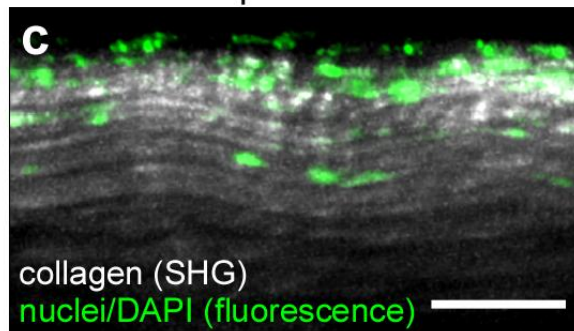
SHG-SPIM



2p-SPIM



2p-SPIM + SHG-SPIM



Supplementary Figure 9

Combined SHG-SPIM and 2p-SPIM imaging of mouse tail

Second harmonic generation (SHG) signal from collagen (**a**) and two-photon fluorescence from DAPI-stained nuclei (**b**) of a mouse tail were collected using the same light-sheet microscopy setup. The images have the axial (*z*) dimension along the vertical axis, showing that the characteristic corrugation structure of collagen fibers could be detected with SHG-SPIM up to depth of $\sim 100\ \mu\text{m}$. (**c**) shows the combined view of the two signals. Excitation wavelength was at 798 nm, and the SHG and DAPI signals were collected with detection spectral bandpass of 395/11 nm and 485/70 nm, respectively. Sample schematics (top of figure): red plane denotes the light-sheet, gray plane denotes the computational slice of the 3D dataset shown in the images, and gray and green arrows denote the signal detection direction. Scale bar, 50 μm .

Supplementary Table 1

Imaging parameters for all the presented images and videos

	Fig. 2a	Fig. 2d	Fig. 2b	Fig. 2e	Fig. 2c,f
Modality	2p-SPIM	2p-SPIM	1p-SPIM	1p-SPIM	2p-LSM
Sample	Fly, stage 13				
Imaged volume (xyz) (voxels)	400x900x170	400x900x170	400x900x170	400x900x170	400x900x170
Lateral pixel size (μm)	0.635	0.635	0.635	0.635	0.63
Axial section (z-step) size (μm)	1	1	1	1	1
Excitation wavelength (nm)	940	940	488	488	940
Unidirectional power (mW)	100	100	0.2	0.2	40 ([^])
Bidirectional illumination	yes	no	yes	no	n/a
Exposure time, frame (ms)	150	150	150	150	1000
Excitation rejection filter	SP750	SP750	n/a	n/a	SP680
Detection bandpass filter	BP525/50	BP525/50	BP525/50	BP525/50	BP525/50

	Fig. 2g, Supp. Fig. 4a,b,g Supp. Video 2	Fig. 2h, Supp. Fig. 4c,d,h	Fig. 2i, Supp. Fig. 4e,f,i	Supp. Fig. 2	Supp. Fig. 6b Supp. Videos 4-6
Modality	2p-SPIM	1p-SPIM	2p-LSM	2p-SPIM	2p-SPIM
Sample	Fly, stage 5	Fly, stage 5	Fly, stage 5	Fly, stage 5	Fly, stage 16
Imaged volume (xyz) (voxels)	400x900x150	400x900x150	400x900x150	400x900x100	400x900x120
Lateral pixel size (μm)	0.635	0.635	0.63	0.635	0.635
Axial section (z-step) (μm)	1	1	1	1	1
Excitation wavelength (nm)	940	488	940	940	940
Unidirectional power (mW)	100	0.2	40*	30	100
Bidirectional illumination	yes	yes	n/a	yes	yes
Exposure time, frame (ms)	150	150	1000	1000	100
Excitation rejection filter	SP750	n/a	SP680	SP750	SP750
Detection bandpass filter	BP525/50	BP525/50	BP525/50	BP525/50	BP525/50

	Supp. Fig. 6b Supp. Videos 4-5	Supp. Fig. 8 Supp. Video 7	Supp. Fig. 9a	Supp. Fig. 9b	Supp. Video 3
Modality	1p-SPIM	2p-SPIM	SHG-SPIM	2p-SPIM	2p-SPIM
Sample	Fly, stage 16	Zebrafish	Mouse tail	Mouse tail	Fly
Imaged volume (xyz) (voxels)	400x900x120	400x400x1	500x1000x150	500x1000x150	200x450x190
Lateral pixel size (μm)	0.635	0.4	0.635	0.635	1.27
Axial section (z-step) (μm)	1	n/a	1	1	1
Excitation wavelength (nm)	488	920	798	798	940
Unidirectional power (mW)	0.2	50	100	100	100
Bidirectional illumination	no	no	yes	yes	yes
Exposure time, frame (ms)	100	13.9	200	100	100
Excitation rejection filter	n/a	SP750	SP750	SP750	SP750
Detection bandpass filter	BP525/50	BP525/50	BP395/11	BP485/70	BP525/50

Supplementary Table 1

Imaging parameters for all the presented images and videos

Identical imaging parameters between **Fig. 2j** (stage 8 and 13) and **Supplementary Video 3**; between **Fig 2j** (stage 16) and **Supplementary Fig. 6b**. ([^]) For 2p-LSM imaging of flies, the phototoxicity threshold of excitation power is ~ 30 mW for continuous 3D imaging for extended time duration (1 hour or more)¹⁰. Imaging of individual z-stacks could tolerate higher level of excitation power.

Supplementary Results 1

Resolution characterization

In comparing the imaging performance of the three imaging modalities of 2p-SPIM, 1p-SPIM, and 2p-LSM, the imaging setups were initially adjusted, via control of illumination NA and pixel sampling size, to achieve the same resolution of $\sim 1 \mu\text{m}$ laterally and $\sim 2 \mu\text{m}$ axially in imaging an ideal sample of sub-diffraction fluorescent beads (diameter = 170 nm, Molecular Probes) embedded in clear agarose gel. These resolution parameters were chosen for optimal imaging of the nuclear-labeled fly embryos, as these have nuclei of size $\sim 5 \mu\text{m}$. For the resolution characterization experiments, the wavelength for 2p (1p) excitation was 940 (488) nm, and the fluorescence from the beads was centered around 520 nm. Neglecting the finite size of the beads, the point spread function resolution for each imaging modality was found by analyzing the 3D image of the beads (**Supplementary Fig. 1b**) following the procedure described in²², yielding the FWHM values as follow: 2p-SPIM: $\Delta x, y = 1.3 \pm 0.20 \mu\text{m}$, $\Delta z = 2.0 \pm 0.33 \mu\text{m}$; 1p-SPIM: $\Delta x, y = 1.2 \pm 0.16 \mu\text{m}$, $\Delta z = 2.2 \pm 0.30 \mu\text{m}$; 2p-LSM: $\Delta x, y = 1.3 \pm 0.23 \mu\text{m}$, $\Delta z = 1.8 \pm 0.26 \mu\text{m}$. To reach these resolution parameters, the NA used in 2p- and 1p-SPIM were estimated to be ~ 0.08 and 0.06 , respectively, yielding a fluorescence light-sheet with FWHM of $\sim 3 \mu\text{m}$ (Eqs.(6) & (8) of **Supplementary Discussion 1**), and a bidirectional field of view of $b \sim 250 \mu\text{m}$ (Eq. (5) of **Supplementary Discussion 1**).

The observed lateral resolutions of all three imaging modalities were determined by the pixel sampling size, rather than optically. For 2p and 1p-SPIM, with the 20X detection lens coupled with a 0.63X demagnification adapter, the 8-um camera pixel size corresponds to a pixel size of $0.635 \mu\text{m}$ at the sample plane, which yields an effective imaging resolution of $2 \times 0.635 = 1.27 \mu\text{m}$ (according to the Nyquist criterion), which was approximately what we observed. For 2p-LSM, the point-scanning pixel size was set at $0.63 \mu\text{m}$, which would yield an effective resolution of $1.3 \mu\text{m}$, as was observed. The observed axial resolutions of all three imaging modalities was larger than what was expected optically from the $\text{NA} = 1.0$ of the objective lens used²²⁻²³ - this was expected since the (Zeiss W Plan-Apochromat 20X, $\text{NA} = 1.0$) objective lens has an unusually large back aperture that was not fully utilized in our experimental setups.

For 2p-LSM, to reach an axial resolution $\Delta z = 2 \mu\text{m}$, the same as experimentally reached in 2p-SPIM, requires a focusing NA of 0.83 , following²³. Thus, we see that to reach approximately the same axial resolution of $2 \mu\text{m}$, 2p-SPIM uses a focusing NA that is smaller compared to that used in 2p-LSM by: $0.83/0.08 \sim 10$ fold.

Supplementary Results 2

Similar signal rate of 2p-SPIM and 2p-LSM

Because of the orthogonal geometry between the illumination and detection directions in a light-sheet setup, to reach the same resolution, the illumination NA used in SPIM is substantially smaller than in conventional microscopy. In our case, the NA employed in 2p-SPIM is smaller by a factor of 10 compared with 2p-LSM, raising intuitive concerns about whether sufficient nonlinear fluorescent signal can be generated in 2p-SPIM, as compared to 2p-LSM, without using phototoxic levels of laser power. However, with a spherically-focused beam, the average excitation probability within the focal volume for 2p excitation is proportional to NA^4 , and the total focal volume is proportional to NA^{-4} , hence the total excitation (given by the excitation probability times the focal volume) is independent of the focusing NA for a homogeneous distribution of fluorophores²³. Thus, 2p-SPIM and conventional 2p-LSM should have the same average signal rate in imaging an extended 3D sample, under the same average laser excitation power, spatial sampling density (voxel size), and detection efficiency. This somewhat counter-intuitive result could be understood in another way by noting that even though for 2p-LSM the instantaneous signal rate at each voxel is higher due to the tighter focusing, these voxels are illuminated one at a time, while in 2p-SPIM an entire row of voxels is effectively illuminated and imaged simultaneously. Hence longer voxel exposure time could be used in 2p-SPIM to compensate for the lower instantaneous signal rate, making the final signal rate equal for the two modalities. We verified this result experimentally by imaging a live fly embryo with 2p-SPIM, using imaging parameters that are typically used for 2p-LSM¹⁰ (acquisition time of 1 sec for frame of 400 x 900 pixels, and total average power of 30 mW at the sample). The acquired images (**Supplementary Fig. 2**) have approximately the same signal quality as that obtained through 2p-LSM with similar imaging parameters and samples¹⁰.

Supplementary Results 3

Quantification of imaging depth via analysis of images in Fourier space

To compare the imaging penetration depth achieved by the three different imaging modalities considered in our study, we analyzed the 3D embryo imaging datasets in the spatial frequency domain based on Fourier analysis. With the z- and x-directions denoting the detection and illumination directions in light-sheet microscopy (**Fig. 1a-c** and **Supplementary Fig. 5a**), we want to investigate the penetration depth in either the detection direction (from z-stacks of xy-slices) or in the illumination direction (from x-stacks of yz-slices). Hence, the 2D discrete Fourier transform F from xy- or yz-slices of the 3D datasets were calculated using Matlab 2D-fast Fourier transform (FFT) algorithm. In the following, we describe Fourier analysis of xy-slices; the same analysis was performed using the yz-slices (**Supplementary Fig. 5b,c**).

We calculated the normalized xy-Fourier spectra from individual image slices as $|F(v_x, v_y)|/|F(0,0)|$ with the spatial frequencies v_x and v_y in units of μm^{-1} , corresponding to spatial wavelengths of $\lambda_x = 1/v_x$ and $\lambda_y = 1/v_y$. Representative spectra are displayed, together with the corresponding images, using a logarithmic scale in **Supplementary Fig. 5c**.

We define a metric called the useful contrast to quantify the image quality (**Supplementary Fig. 5b**). It is specific for each spatial direction and is given by $\langle |F| \rangle_x / \langle |F| \rangle$ and $\langle |F| \rangle_y / \langle |F| \rangle$, in x- and y-direction, respectively. $\langle |F| \rangle_x$ and $\langle |F| \rangle_y$ are the average Fourier spectrum coefficients in the spatial frequency range defined in **Supplementary Fig. 5b** (with $0.05 < v < 0.4 \mu\text{m}^{-1}$, corresponding to $2.5 < \lambda < 20 \mu\text{m}$). They are normalized by $\langle |F| \rangle$, the average Fourier spectrum coefficients in the entire xy image slice. The spatial frequency range in the definition of the useful contrast corresponds to structures in the images with biologically relevant information: as illustrated in **Supplementary Fig. 5c**, filtering the fly images in the Fourier domain by attenuating the Fourier coefficients in the wavelength range defined above ($2.5 < \lambda < 20 \mu\text{m}$) drastically reduced the signal from the nuclei and leave only high-frequency noise and low-frequency background (see Image 4 analysis in **Supplementary Fig. 5c** compared to Image 1 before filtering).

More generally, **Supplementary Fig. 5c** illustrates how the useful contrast values quantify image quality by comparing 5 different sample cases: Images 1, 2 and 3 are the images from **Supplementary Figs. 4b, 4d, and 4f**, respectively (i.e., 2p-SPIM, 1p-SPIM, and 2p-LSM, respectively). Image 4 is the Fourier filtered image of Image 1 for which Fourier coefficients in the $0.05 < v < 0.4 \mu\text{m}^{-1}$ range are lowered by a factor of 5. Finally, Image 5 is a computer-generated white noise image using Matlab rand function. By definition, the value of the useful contrast approaches one as the image has less useful information and becomes dominated by noise and background (Images 4 and 5). Anisotropic resolution is highlighted by different values of useful contrast in each spatial direction (see the differences between Images 1 to 3). The yz-Fourier analysis presented in **Supplementary Fig. 5c** demonstrates the 2p-SPIM spatial resolution is more isotropic in y and z directions than 1p-SPIM and 2p-LSM. The yz-Fourier spectra plotted in each case in **Supplementary Fig. 5c** confirm that 2p-SPIM exhibit quasi-isotropic signal from the nuclei (yellow circle in the yz-Fourier spectrum of Image 1), while 1p-SPIM and 2p-LSM spectra are clearly anisotropic. Back in the spatial domain, the low z-resolution in Image 3 prevents resolving the nuclei in this direction, whereas they can be resolved in the y-direction. Finally, **Supplementary Fig. 5c** illustrates how the useful contrast allows us to quantify the image quality of a given 2D image using only two numerical values (in each spatial direction); this is critical to analyze image stacks, taken of real biological samples, without requiring inspecting each Fourier spectrum individually. As plotted in the

graphs of **Fig. 1d-e**, for each z-stack (or x-stack), the useful contrast is computed in x- and y-direction (or y- and z-direction) for each xy-slice (or yz-slice) and plotted as functions of z-depth (or x-depth).

It is important to note that the useful contrast as defined here is a single metric characterizing simultaneously the spatial resolution, contrast, and signal to noise ratio (SNR), for a specific spatial direction. It discriminates biologically relevant spatial signal from high-frequency noise (responsible for low SNR) and from low frequency background (responsible for low contrast). In addition, by definition it is sensitive to spatial resolution degradation affecting the biological information. Using such a metric is critical in comparing the three imaging modalities of 2p-SPIM, 1p-SPIM and 2p-LSM: often a metric that quantifies only one single aspect of the image quality is inadequate for comparing the performance of different imaging modalities. For instance, average signal intensity is usually used to characterize depth penetration in 2p-LSM¹⁰ as, in this case, the 2p-excitation guarantees that high signal level is linked to high spatial resolution. However, in the case of 1p-SPIM, the light-sheet spatial thickening at high sample depth results in low spatial resolution with high background, yielding high signal intensity but with low contrast. Hence, signal intensity alone is not a good metric for characterizing the imaging depth performance in 1p-SPIM, or for comparing it with 2p-LSM¹⁴. Contrast alone has been used to characterize 1p-SPIM¹⁴, which is adequate if high-frequency noise is not an issue. As such noise can be a limitation in 2p-LSM, contrast alone then is not adequate for comparing 2p-LSM with SPIM techniques. Thus, it is critical that in experimentally comparing the performance of 2p-SPIM, 1p-SPIM, and 2p-LSM, a metric such as the useful contrast has to be used, to quantify simultaneously the spatial resolution, contrast, and SNR.

In **Fig. 1d** and **Fig. 1e**, the variations of useful contrasts calculated from xy- and yz-slices, respectively, are plotted as functions of sample depth in the light-sheet detection and illumination directions (z- and x-directions, respectively), for 3D datasets similar to those presented in **Fig. 2d-f**, and averaged over six samples for each of the imaging modality. The xy-Fourier analysis (**Fig. 1d**) shows the useful contrast is the same between the lateral dimensions (x and y), as expected, since they are equivalent in the detection, for all three imaging modalities. Following the x- or y-useful contrast as a function of detection z-depth, 2p-SPIM always performs better than 1p-SPIM, and tracks closely with 2p-LSM until about one-third into the embryo, from which point on 2p-LSM has the best lateral useful contrast among the three techniques. The same analysis performed on x-stacks of yz-slices (yz-Fourier analysis in **Fig. 1e**) first confirms that the y- and z-useful contrast of 2p-LSM (gray curves) are approximately independent of the x-depth: this is expected since illumination and detection do not depend on the x-position in this modality. On the contrary, the y- and z-useful contrasts of 2p- and 1p-SPIM (red and blue curves) show the strong dependence on x-depth due to the degradation of the light-sheet illumination when penetrating deeper in this direction (recall that the SPIM datasets being analyzed were taken with illumination coming from only one side along the positive x-direction (schematic below in **Fig. 2d-f**). Secondly, we see that the z-useful contrast is always lower than the y-useful contrast, for all imaging modalities, signifying that axial resolution is always worse than lateral resolution. However, whereas these values are strongly different in the cases 1p-SPIM (blue curves) and 2p-LSM (gray curves), they are closer in the case of 2p-SPIM (red curves), demonstrating the more homogenous image quality of 2p-SPIM data. Finally, we see that among the three modalities, 2p-LSM maintains the best lateral useful contrast (y-direction) while 2p-SPIM has the best axial useful contrast (z-direction). Together, these results demonstrate the high performance of 2p-SPIM in maintaining good resolution and contrast in depth, especially in the axial direction, making it the best among the three modalities in approaching the ideal isotropic resolution for imaging a 3D sample. Taking the depth penetration, along z or x-direction, as the depth where the useful

contrast remains at a particular level above the noise, we conclude from this analysis that for the highly scattering fly embryo sample, the penetration depth of 2p-SPIM is, on average, about 2 times better than that of 1p-SPIM, and is competitive with that of 2p-LSM (performing worse laterally but better axially).

Supplementary Results 4

Analysis of fly photodamage experiments

We investigated the photodamage induced by the long-term 2p-SPIM imaging procedure applied to fly embryos and described in **Online Methods** by analyzing the overall survival of embryos until hatching, the timed sequence of developmental stages, the phenotypic signs of phototoxicity, and the fluorophore photobleaching.

80% of control non-illuminated embryos ($n = 109$, see **Online Methods**) developed normally until before hatching (evidenced by the movement of the fully-formed larva trying to break out of the vitelline membrane), and 70% succeeded in hatching. These rates of normal development and hatching are similar to those we observed previously with the same glue-mounting procedure¹⁰. For the illuminated embryos at the power level of 200 mW ($n = 6$) (embryos 1-6 in **Fig. 3a** and **Supplementary Fig. 7**), 100% developed normally until before hatching, and 80% succeeded in breaking the vitelline membrane. Both embryos illuminated with 150 mW (embryo 7-8) developed normally and hatched. Observation of the approximately 18-hour 3D time-lapses of all the illuminated embryos (**Supplementary Fig. 7**, a representative time-lapse is shown in **Supplementary Video 3**) found that the development of all embryos had proceeded normally, undergoing the normal timed sequence of development (**Fig. 3a**) as compared to the literature (for instance, see The Interactive Fly website: <http://www.sdbonline.org/fly/aimain/1aahome.htm>). Each developmental event was fairly synchronized between embryos (**Fig. 3a**). In addition, no phenotypic signs of phototoxicity were observed, such as increased cell deaths, embryo shrinkage, disrupted morphogenetic movements, or lack of muscle contractions during the last few hours of development. Importantly, we found no difference between embryos imaged with lower laser power (150 mW, embryos 7-8) versus the higher laser power (200 mW, embryos 1-6) - a difference in the timed sequence of development would be expected between these embryos if we were operating at or near the threshold of phototoxicity.

To analyze the photobleaching, we plotted the relative fluorescence signal as a function of development time (**Fig. 3b**). We found no decrease of the fluorescence signal for the entire 18-hour time-lapse, after more than 2500 cycles of z-stack image acquisitions. The total signal actually showed an overall increase from the beginning of gastrulation to the end of embryonic development - which could be explained by the production of H2A-GFP and/or changes in tissue optical properties.

Supplementary Results 5

Second harmonic generation scanned light-sheet microscopy

A useful feature of a conventional 2p-LSM setup is that it can be used to combine fluorescence with harmonic generation imaging, where image contrast is generated by nonlinear scattering of light by the biological structures themselves, without requiring exogenous labeling. The combination of 2p-LSM with second and third harmonic generation LSM has been recently applied for extended 4D imaging of developing embryos²⁶. We show the multi-modality of our 2p-SPIM setup by straightforwardly extending it to second harmonic generation scanned light-sheet microscopy (SHG-SPIM). SHG, where the signal photon has exactly twice the energy (or half the wavelength) of the excitation photon, is generated from the non-centrosymmetry exhibited in various endogenous biological molecules, including many structural components such as collagen²⁵. We imaged mouse tail tissue on the same light-sheet setup combining two contrast mechanisms: SHG signal from the collagen fibers and 2p-excited fluorescence signal from labeled cell nuclei (**Supplementary Fig. 9**). SHG signal is generally mostly directed toward the illumination optical axis due to coherent mechanisms, though complex arrangements of SHG-active scatterers at the sub-wavelength scale could produce signal directed at substantial angles away from the illumination axis²⁵ which would be detected in the light-sheet geometry.

Supplementary Discussion 1

Resolution and field of view in 2p- and 1p-SPIM

In SPIM, the lateral and axial resolutions of the final image are decoupled: lateral resolution is determined by the detection optics alone, while the axial resolution is determined by both the thickness of the light-sheet and the detection optics. The thickness of the light-sheet is the key in providing the axial sectioning in SPIM – as the sheet becomes thicker, the imaging is reduced to conventional wide-field imaging with its inherent lack of axial sectioning due to the blurring effect of out-of-focus light. The focusing property of the illumination light could be well approximated by paraxial Gaussian beam optics. Referring to **Supplementary Fig. 1a** and its inset, the intensity profile of the beam is described by:

$$I(r, x) = \frac{2P}{\pi w^2} e^{-2r^2/w^2} \quad (1)$$

where P is the total laser power, r is the radial dimension in the yz -plane, x is the propagation direction of the illumination beam (defined to be zero at the focal point), and the beam waist parameter w is given by:

$$w(x) = w_0 \left[1 + \left(\frac{\lambda x}{n\pi w_0^2} \right)^2 \right]^{1/2} \quad (2)$$

$$w_0 = \frac{\lambda}{\pi(NA)} \quad (3)$$

$$FWHM = \sqrt{2 \ln 2} \cdot w_0 \quad (4)$$

with λ being the light wavelength in vacuum, n the medium refractive index, NA the focusing numerical aperture ($NA \equiv n \sin \theta$ where θ is the half focusing angle), w_0 is the (e^{-2}) radius of the beam profile at the focal point, and the full width half maximum ($FWHM$) of the beam profile is often used to designate the minimum lateral size that a diffraction-limited focused beam of light can reach. In SPIM microscopy, the lateral $FWHM$ of the illumination focus, together with the detection objective lens axial point spread function, determines the axial resolution (along the z -direction) of the final image captured by the camera. The field of view of SPIM is defined as the extent in the x -dimension about the focal point where the thickness of the light-sheet remains below a certain threshold, ensuring that the imaging axial resolution is approximately uniform over the field of view. If this thickness threshold is taken as $\sqrt{2} \cdot w_0$, then the field of view is equal to b , the confocal parameter of the illumination focus:

$$b = \frac{n\pi w_0^2}{\lambda} = \frac{2n\lambda}{\pi(NA)^2} \quad (5)$$

The fluorescence signal rate of 1p-SPIM is proportional to the illumination light intensity, $S_{1p} \propto I$, and hence has the same $FWHM$, thus the fluorescence light-sheet of 1p-SPIM has thickness:

$$FWHM_{1p} = \frac{\sqrt{2 \ln 2} \cdot \lambda_{1p}}{\pi(NA_{1p})} \quad (6)$$

The fluorescence signal rate of 2p-SPIM is proportional to the squared of the illumination light intensity:

$$S_{2p} \propto I^2 \propto \frac{4P^2}{\pi^2 w^4} e^{-2r^2/(w/\sqrt{2})^2} \quad (7)$$

Thus the radial spatial profile of S_{2p} is also a Gaussian but with the intrinsic width reduced by a factor of $\sqrt{2}$ compared to that of the illumination profile. Then the fluorescence light-sheet of 2p-SPIM has thickness:

$$FWHM_{2p} = \frac{\sqrt{\ln 2} \cdot \lambda_{2p}}{\pi(NA_{2p})} \quad (8)$$

Since the illumination wavelength in 2p- is about 2 times that in 1p-SPIM, $\lambda_{2p} \approx 2 \cdot \lambda_{1p}$, if we want to reach the same axial resolution with the two modalities, i.e. the same *FWHM* in Eqs. (6) and (8), then we have to use $\sqrt{2}$ times larger NA for 2p-SPIM, $NA_{2p} \approx \sqrt{2} \cdot NA_{1p}$. Note that for $FWHM_{2p} = FWHM_{1p}$ then the field of view (Eq. (5)) is the same for the two modalities. The finite variation of the light-sheet thickness across the field of view leads to a spatial variation in the average signal: the ratio of the average signal at the center versus at the edge is 2 and 4, for 1p- and 2p-SPIM, respectively. This variation, which is usually well accommodated by the high dynamic range of CCD cameras, needs to be taken into account in any quantitative analysis of the captured image.

Supplementary Discussion 2

Advantages of the scanned light-sheet versus static light-sheet for 2p-SPIM

The implementation of the light-sheet via fast scanning of a spherically-focused light beam⁶ used in our setup has distinct advantages over the implementation of a static light-sheet via focusing with a cylindrical lens, as is typically done in SPIM. Reference⁶ already described the benefits of the scanned light-sheet in achieving higher excitation power throughput, better spatial uniformity in the y-dimension of the field of view (refer to imaging geometry in **Supplementary Fig. 1**), and allowing convenient execution of non-coherent structured illumination to improve signal contrast¹⁴. In addition, it has been recently demonstrated that the scanned light-sheet minimizes scattering artefacts compared to the static light-sheet illumination used in SPIM¹⁶. All of these benefits exist in both 1p- and 2p-SPIM. For the latter case, the spherically-focused scanned light-sheet yields an additional critical benefit over the cylindrically-focused static light-sheet, in producing significantly more nonlinearly-excited fluorescence signal for the same average excitation power. This can be seen in the following analysis.

Referring to the coordinate system definition in **Supplementary Fig. 1** and its inset, we consider a comparison between a scanned light-sheet spherically focused to a certain characteristic width w_0 in both the z- and y-directions, and a static light-sheet cylindrically focused to the same width w_0 in the z direction while being uniform in the y direction over a range of Nw_0 , with N being a positive real number. Nw_0 denotes the extent of the field of view in the y-direction (in our experimental implementation, $N \simeq 200$, yielding a field of view of about $600\mu\text{m}$ with $w_0 \simeq 3\mu\text{m}$). The excitation intensity is proportional to the average excitation power divided by the beam cross-sectional area, and thus is given by:

$$I \propto \frac{P}{w_0^2} \quad (\text{scanned sheet}) \quad (9)$$

$$I' \propto \frac{P}{Nw_0^2} \quad (\text{static sheet}) \quad (10)$$

where P is the same average excitation power used in both cases. The 2p-excited fluorescence signal rate, which is proportional to the squared of the intensity, averaged over the full extent of Nw_0 along the y-direction, is then:

$$S \propto \frac{1}{N} \cdot \frac{P^2}{w_0^4} \quad (\text{scanned sheet}) \quad (11)$$

$$S' \propto \frac{1}{N^2} \cdot \frac{P^2}{w_0^4} \quad (\text{static sheet}) \quad (12)$$

The factor $(1/N)$ in the expression of the signal in Eq. (11) above reflects the scanning that has to be done for the w_0 -wide beam to cover the Nw_0 -wide field of view along the y-direction, producing an effective spatial duty cycle of $(1/N)$. We see then from Eqs. (11) and (12) that, with the same average excitation power, the average signal in the scanned sheet case is a factor of N larger than in the static sheet case. This comes directly from the quadratic dependence of the 2p-excited fluorescence signal on the excitation intensity. Since experimentally N is in the range of a few hundred, the difference between the two signals is significant.

The scanned light-sheet was generated in our setup by fast scanning of the beam, with period of 1 ms to cover the full field of view. This kHz-speed is fast enough to produce an effectively uniform illumination intensity across the y-extent of the field of view, for imaging exposure times of tens of ms or more, as were the case in our work. For shorter exposure times, faster scanning hardware could be employed (e.g. resonant scanners or spinning polygon mirrors can scan in the range of 10-100 kHz).

Supplementary Discussion 3

Low photodamage of 2p-SPIM allows high speed imaging

In discussing photodamage, it is useful to classify the photodamage effects into three categories: linear, quadratic, and supra-quadratic, which corresponds to effects that come from absorption of one, two, and more than two photons, respectively. If we write photodamage $\propto I^m$, with I being the peak intensity of the excitation light, then $m = 1, 2,$ and >2 , for the linear, quadratic, and supra-quadratic photodamage, respectively.

One general feature of SPIM making it less photodamaging, compared to conventional microscopy techniques, is that due to its unique orthogonal illumination, the excitation light irradiates only the focal plane that is being observed. With conventional microscopy techniques, where the excitation and detection are collinear, the irradiated light necessarily passes through the entire sample even as information is collected from only one focal plane. Thus, for imaging of a 3D sample composed of n z-slices, SPIM would expose the sample to n times less total light energy than conventional microscopes. Since away from the focal plane, the excitation light intensity would be too weak for any appreciable nonlinear absorption, the single-plane illumination feature mainly reduces the linear photodamage effects for 2p-SPIM. Thus, for 2p excitation with NIR wavelengths, the single-plane illumination would help 2p-SPIM to have less linear toxicity effect due to water absorption in the NIR range compared to conventional 2p-LSM.

The main feature of 2p-SPIM that makes it less photodamaging than 2p-LSM is the lower illumination focusing NA required for reaching the same resolution. Lower NA means lower peak intensity for the same average excitation power, which means that if we require the same total 2p fluorescence signal, the quadratic phototoxicity effect would be the same, while the super-quadratic effect would be less. There has been mounting experimental evidence (see⁹ and references therein) that supra-quadratic photodamage is the main mechanism for photodamage in nonlinear microscopy of *in vivo* samples. As the intensity scales with the square of the NA, the factor of 10 reduction in NA of 2p-SPIM, giving a factor of 100 reduction in I , should significantly reduce the photodamage of 2p-SPIM compared to 2p-LSM, or conversely, should allow usage of much higher average power while still staying below a certain photodamage threshold, therefore improving the SNR and/or imaging speed, as demonstrated in the main text. Note that the much lower peak intensity of 2p-SPIM, compared to 2p-LSM, also means that excitation saturation is minimized, ensuring that all the gain in excitation power would translate directly to gain in signal.

As we continue to push the acquisition speed and SNR of 2p-SPIM higher by using higher average excitation power, the improvement will be eventually limited by the threshold of power where photodamage is determined mainly by linear or quadratic (involving absorption of one or two photons) rather than supra-quadratic processes. This threshold power is expected to vary for different biological samples, but general considerations suggests that the threshold for toxic heating effects due to linear absorption by water might lie in the few Watts range²⁷. Consideration of toxic linear heating effects also further illustrates the advantage of using a scanned light-sheet, versus a static one, for implementing 2p-SPIM. Even though the lower peak intensity of the static sheet reduces supra-quadratic phototoxicity, its lower signal rate (see **Supplementary Discussion 2**) requires more than ten times higher average power just to produce the same signal level as the scanned sheet. This high power requirement would not only be beyond what commercially-available lasers could provide, but also would likely be higher than the threshold for toxic linear heating.

Supplementary Discussion 4

Comparison of 2p-SPIM with other imaging techniques

The main disadvantage of 2p-SPIM comes from the high cost of ultrafast lasers, though this is ameliorated somewhat by the recent commercial availability of lower-cost fiber-based ultrafast lasers. Cost concerns and an overall less availability of suitable fluorophores also make 2p-SPIM less amenable to multi-color imaging compared to the 1p counterpart. Peak excitation intensity is significantly higher with 2p excitation than with 1p excitation, leading to more potential photodamage in the former case, which ultimately could limit the SNR and/or imaging speed of 2p compared to 1p-SPIM. However, photodamage is generally significantly reduced with the longer wavelengths used in 2p excitation due to the much lower linear excitation of endogenous bio-molecules. So, the question whether 2p- or 1p-SPIM is less photodamaging, and thus more suitable, for a particular imaging application has to be determined on a case by case basis.

The signal rate of 2p-SPIM is similar to that of 2p-LSM because the excitation beam is maintained as one single coherent unit, spatially and temporally, and useful signal is collected over the entire focal volume of the illumination beam. Other strategies that allow parallelized 2p excitation (reviewed in¹⁸) such as multi-focus illumination²⁸, pulse splitting⁹, or temporal focusing²⁹, divide the beam into distinct units in space or in time, or collect useful signal over only a fraction of the focal volume, respectively, and thus have an inherently lower signal rate than 2p-LSM and 2p-SPIM (due to the quadratic dependence of the signal on the intensity). Thus, 2p-SPIM, with its higher signal rate, is expected to compare favorably against these other parallelized 2p-excitation imaging modalities in terms of the potential for fast 4D imaging.

2p-SPIM could be straightforwardly combined with non-coherent structured illumination¹⁴ to further increase the imaging depth. Note that structured illumination and 2p-excitation are complementary approaches in improving the imaging resolution at high sample depths: the former enhances the in-plane contrast of the imaged light-sheet, directly leading to improvement in lateral resolution, while the latter maintains the ideal light-sheet thickness, directly leading to improvement in axial resolution. The use of Bessel beams for light-sheet illumination¹⁶⁻¹⁷ (which very recently has been found to benefit from 2p-excitation¹⁷) increases the ratio of the field of view over the axial resolution beyond the limit of Gaussian beam optics, providing a means to image with isotropic sub-micron resolution¹⁷. Bessel beam illumination necessarily irradiates the sample with significant amount of laser light outside of the imaged region. This results in a lower signal rate (leading to potential increased linear photodamage), and potential increased sensitivity to optical aberrations; both of these effects are expected to be worse for larger samples.

Supplementary References

26. Olivier, N. *et al.*, *Science* **329** (5994), 967 (2010).
27. Schönle, A. and Hell, S., *Opt. Lett.* **23**, 325 (1998).
28. Bewersdorf, J., Pick, R., and Hell, S.W., *Opt. Lett.* **23** (9), 655 (1998).
29. Oron, D., Tal, E., and Silberberg, Y., *Opt. Express* **13** (5), 1468 (2005).